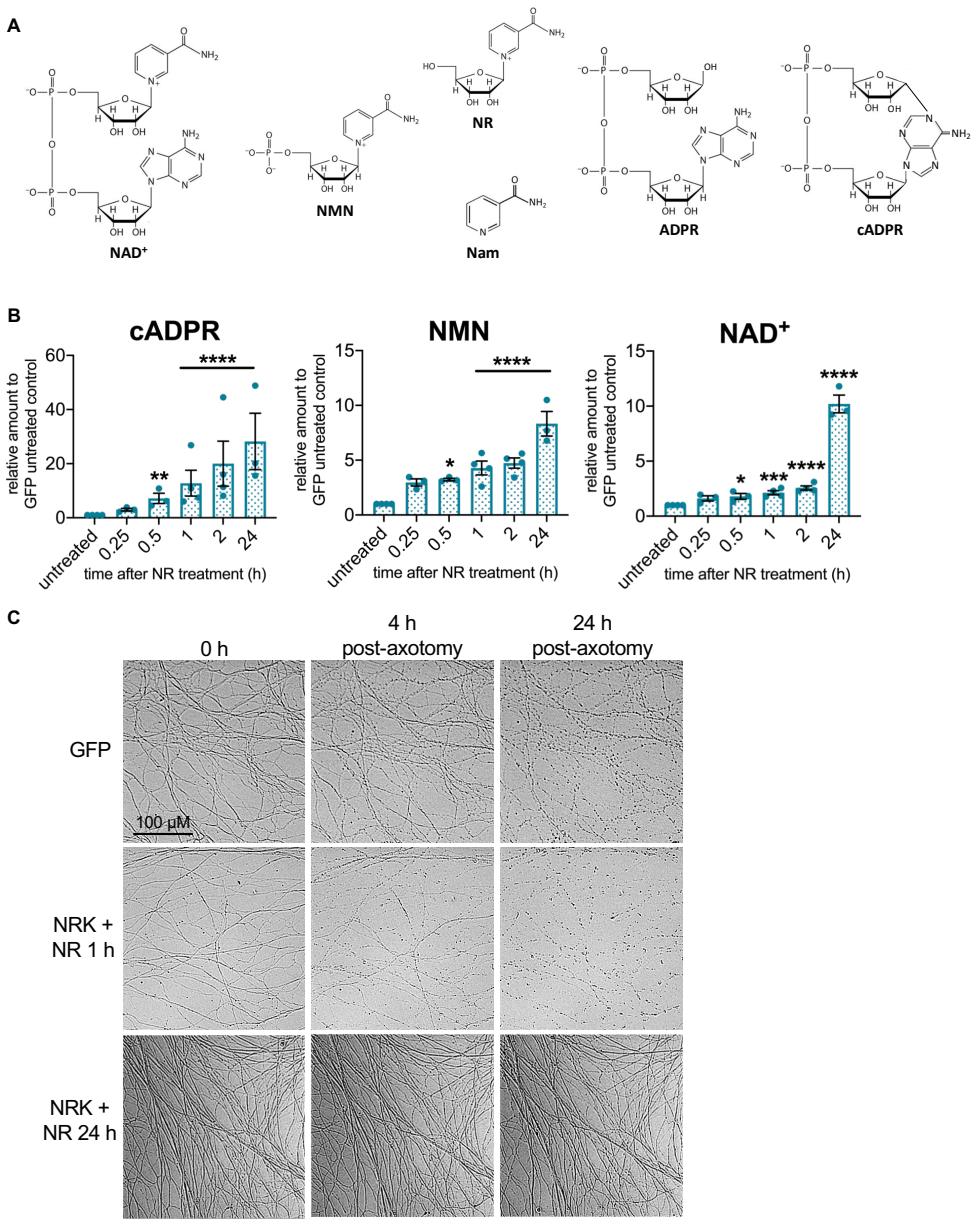

Figure S1: LC-MS-MS measurements from primary neurons treated with NR (Related to Figure 1).

A) 2D structures of NAD^+ and NAD^+-related molecules. **B)** NMN, cADPR and NAD^+ levels in primary eDRG neurons with lentiviral expression of GFP control and treated with NR, as measured by LC-MS-MS. Data correspond to means from replicate experiments and error bars denote ±SEM. Statistical significance was determined by nonparametric Kruskal-Wallis test with Dunn's test for multiple comparisons, comparing each time-point to untreated control. * denotes P value=<0.05; **=<0.01; ***=<0.001; ****=<0.0001. **C)** Representative images of embryonic DRG axons that are quantified in Figure 1D.

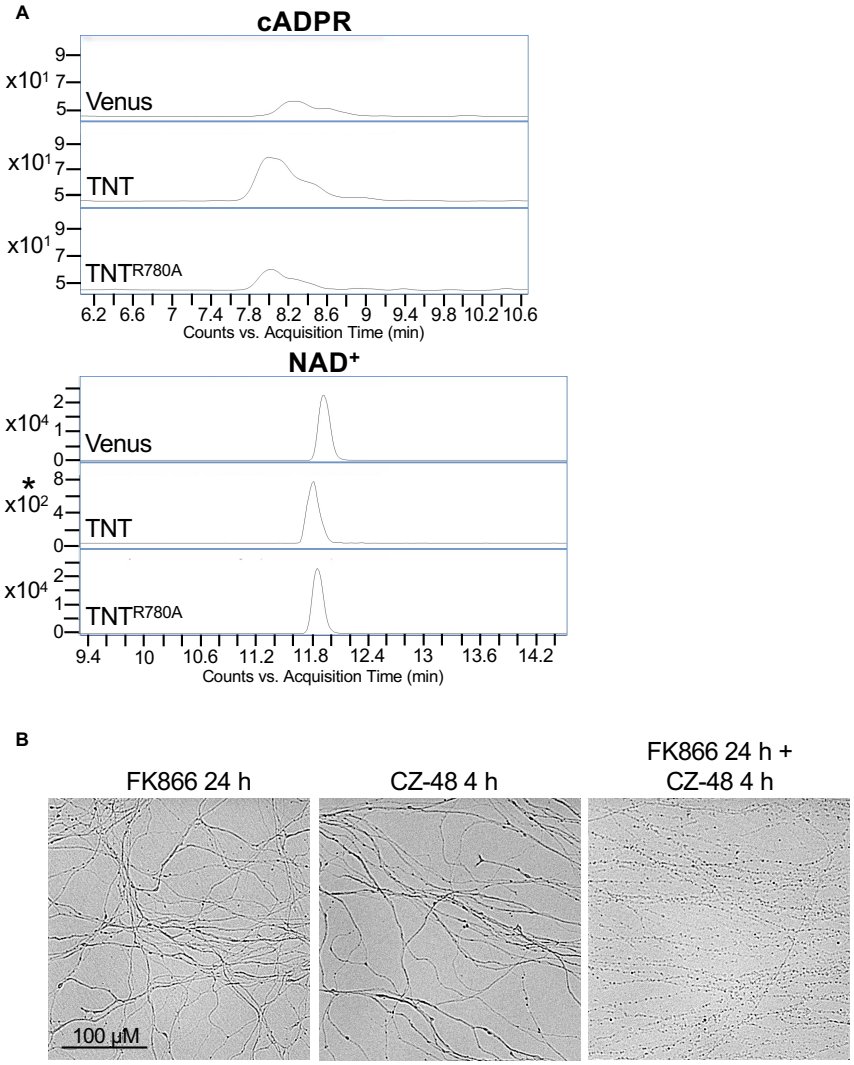

Figure S2: LCMS data and axon images (Related to Figure 2).

A) Representative LCMS peaks for cADPR and NAD^+ collected from primary neurons expressing Venus, TNT, or TNT^{R780A}. For NAD^+, * denotes different Y axis scale (10^2) to show low NAD^+ levels in the TNT condition, compared to 10^4 in Venus and TNT^{R780A} conditions. **B)** Representative images of axons quantified in Figure 2C.

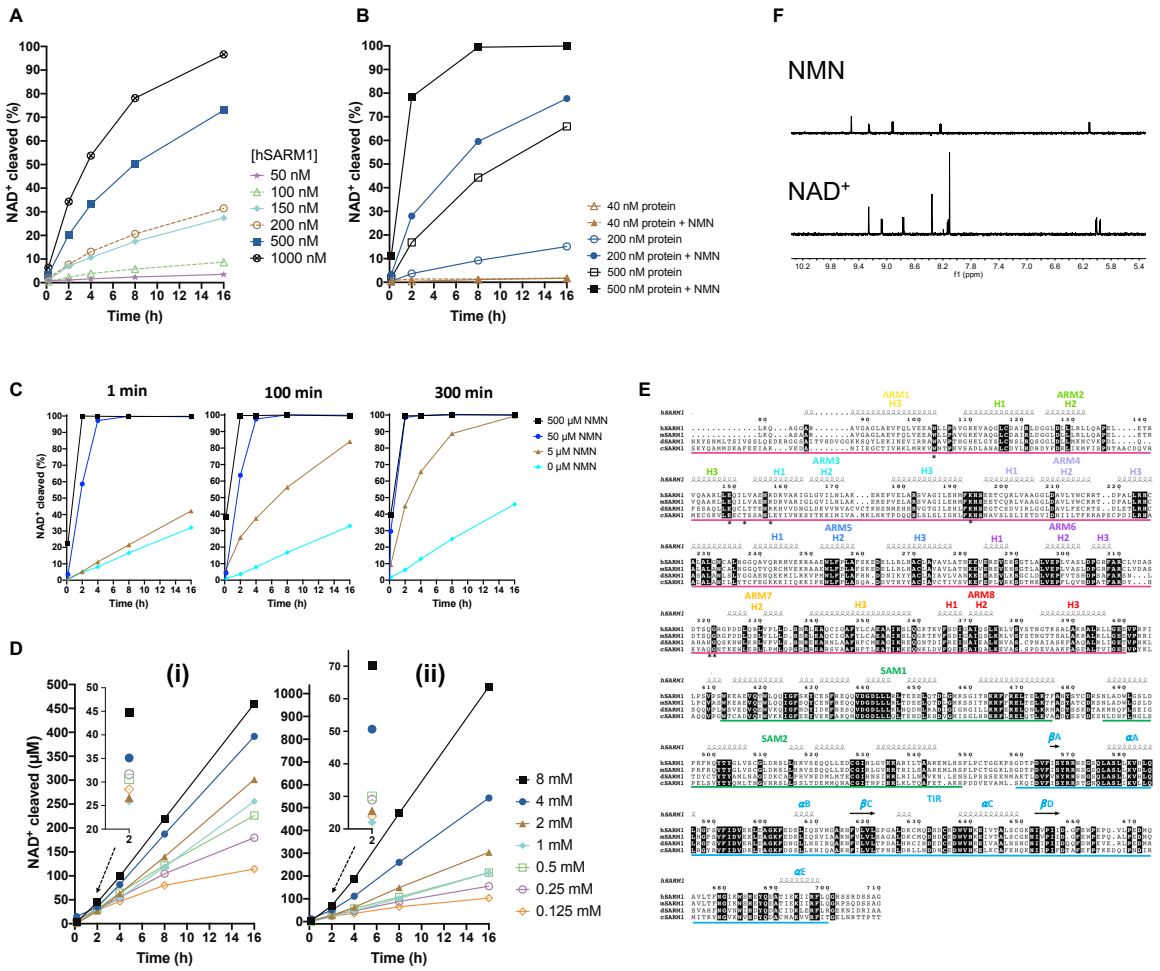

Figure S3: NMR and sequence analyses of SARM1 (Related to Figure 3).

A) NADase activity increases as hSARM1 concentration increases. The initial concentration of NAD^+ was 500 µM for all six samples. **B)** NMN activation of hSARM1 NADase activities at different hSARM1 concentrations. The initial concentration of NAD^+ was 500 µM for all six samples, while an NMN concentration of 500 µM was used for activation. **C)** Different NMN concentrations with 1 min (left panel), 100 min (middle panel) and 300 min (right panel) pre-incubation result in different degrees of activation. The protein concentration was 0.5 µM, while the initial concentration of NAD^+ was 500 µM for all four samples. **D)** NADase activity of hSARM1 with different initial concentrations of NAD^+. Protein concentration was 0.5 µM for all 7 samples. The inset highlights data at the reaction time of 2 h. Two experiments are shown (i and ii). Both experiments show that increased NAD^+ concentration primarily leads to increased NAD^+ cleavage activity. **E)** Sequence alignment of human, mouse, *C. elegans* and *Drosophila* SARM1. The alignment was generated using T-coffee Multiple Sequence Alignment Server (Expresso) (Notredame et al., 2000) and analyzed using ESPript. The ARM, SAM and TIR domains are underlined in magenta, lime and light blue, respectively. Conserved residues are highlighted with black boxes. Residues involved in NMN interaction are indicated by stars. Elements of secondary structure are indicated above the sequence, corresponding to the cryo-EM structure of hSARM1. **F)** STD NMR spectra showing NMN and NAD^+ binding to hSARM1, respectively. The protein concentration was 5.25 µM for both samples, while the initial concentrations of NMN and NAD^+ were both 500 µM. The NAD^+ signals appear to be stronger, a possible result of its weaker binding to the ARM domain.

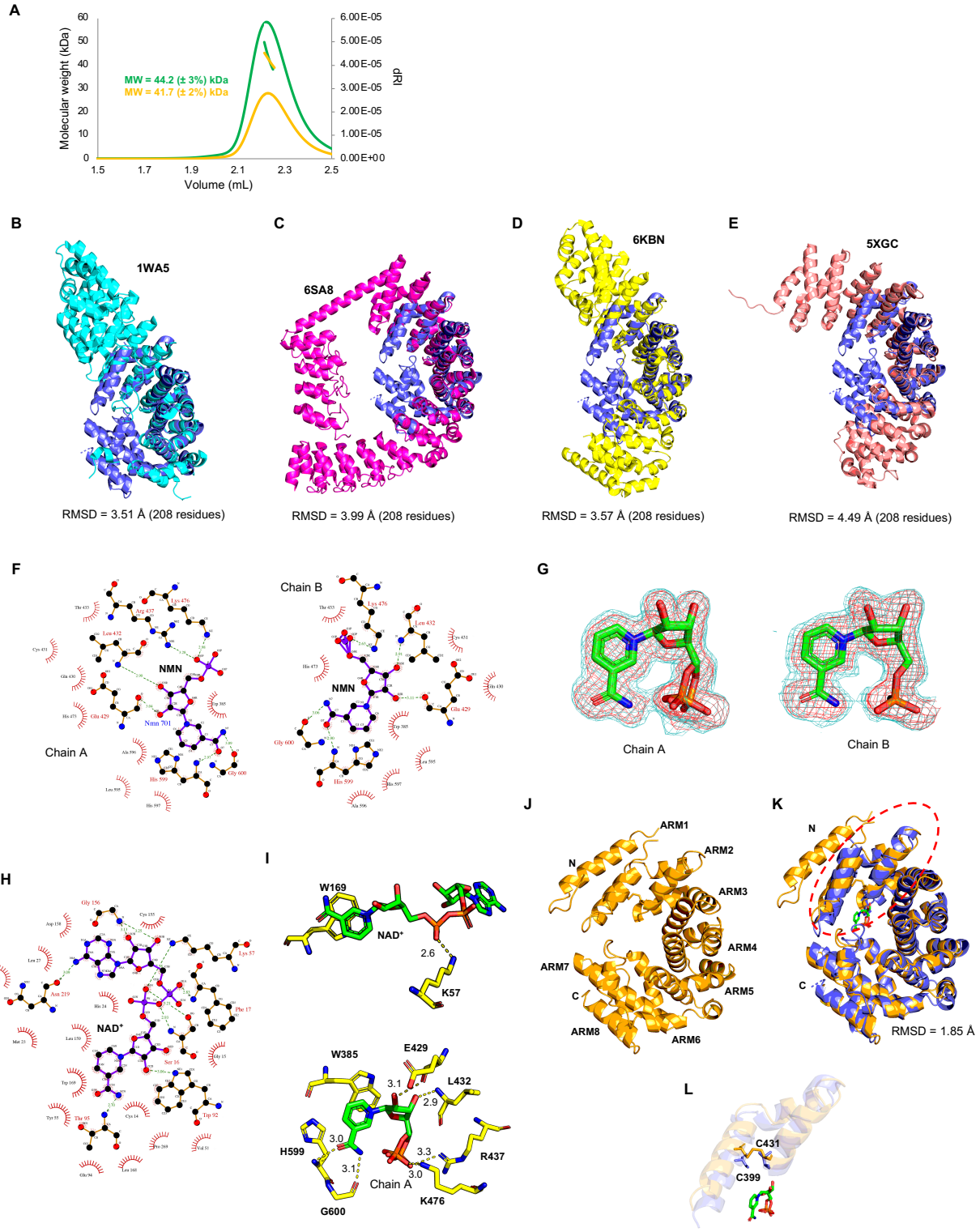

Figure S4: SEC-MALS and structural analyses of dSARM1^{ARM} (Related to Figure 4).

A) SEC-MALS profile of dSARM1^{ARM} in the absence (green) and presence (orange) of NMN. The lines denote the average molecular mass distributions across the peak. The theoretical molecular weight of monomeric dSARM1^{ARM} is 41.2 kDa. **B-E)** The dSARM1^{ARM} protein displays a more compact conformation than previously reported ARM-domain structures. Superpositions (using cealign in PyMOL) of NMN-bound dSARM1^{ARM} (slate) with several ARM domain-containing proteins in ribbon representation: (B) ARM domain from Kap60p (importin-alpha; cyan; PDB: 1WA5; (Matsuura et al., 2004)); (C) ring-like fusion protein with designed armadillo and ankyrin

repeats (magenta; PDB: 6SA8; (Ernst et al., 2019)); (D) vacuolar protein 8 (yellow; PDB: 6KBN; (Park et al., 2020)); (E) small GTPase-GDP dissociation stimulator-558 (pink; PDB: 5XGC; (Shimizu et al., 2017)). **F)** Ligplot diagram of dSARM1^{ARM} interacting with NMN. **G)** Standard omit (red mesh) and Polder (teal mesh) mFo-DFc maps for the NMN molecule in dSARM1^{ARM}. **H)** Ligplot diagram of human NMNAT interacting with NAD^+ (PDB: 1KQN; (Zhou et al., 2002b)). **I)** Stick representation of the interaction between NMNAT and NAD^+ (PDB: 1KQN; (Zhou et al., 2002b)) (top), and between dSARM1^{ARM} (chain A) and NMN (bottom, for comparison). **J)** Cartoon representation of the ligand-free dSARM1^{ARM} crystal structure. **K)** Superposition of the ligand-free (orange) and NMN-bound dSARM1^{ARM} (chain A, slate). **L)** Zoom-in cartoon representation of ARM2 marked with the red dashed circle in panel K, highlighting the cysteines C399 and C431, and NMN in stick representation.

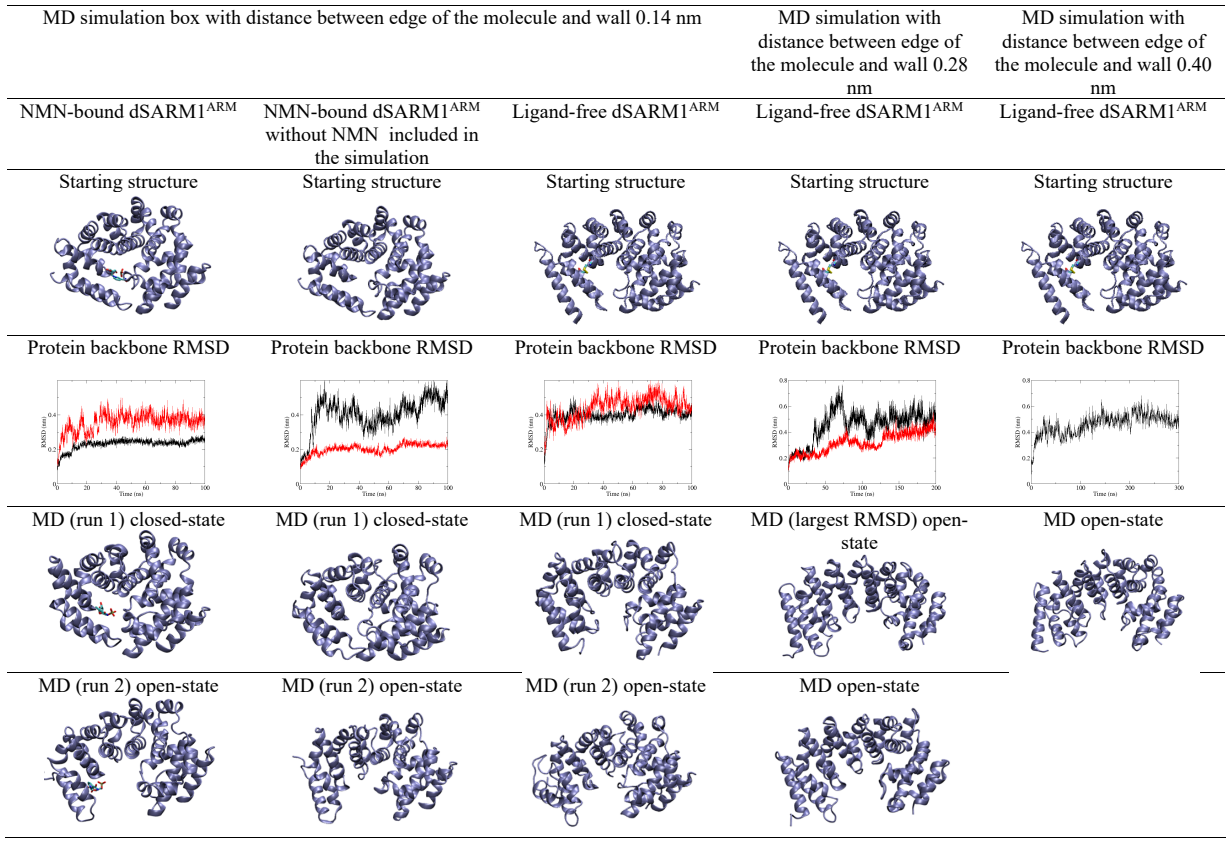

Figure S5: Molecular dynamics simulations of dSARM1^{ARM} (Related to Figure 4).

Starting structures, atom-positional RMSDs of the backbone atoms (C_α, N, C) and final or representative structures of NMN-bound dSARM1^{ARM} (column 1); NMN-bound dSARM1^{ARM} without NMN included in the simulation (column 2); ligand-free dSARM1^{ARM} (column 3) from duplicate 100 ns MD simulations (black and red); ligand-free dSARM1^{ARM} (column 4) from duplicate 200 ns MD simulations (black and red), using a larger MD simulation box; and ligand-free dSARM1^{ARM} (column 5) from 200 ns MD simulations, using the largest MD simulation box. The ligand NMN is shown in stick representation. The disulfide between C399-C431 in the ligand-free crystal (starting) structure is shown in stick representation. No disulfides were included in MD simulations. The MD simulations revealed that both open- and closed-conformations (crystallized state) can be observed for all three systems (column 1-3). In MD simulations performed with ligand-free dSARM1^{ARM} using larger box sizes and longer simulation times (column 4 and 5), the structure opened up within 100 ps and remained in the open-state throughout the simulations.

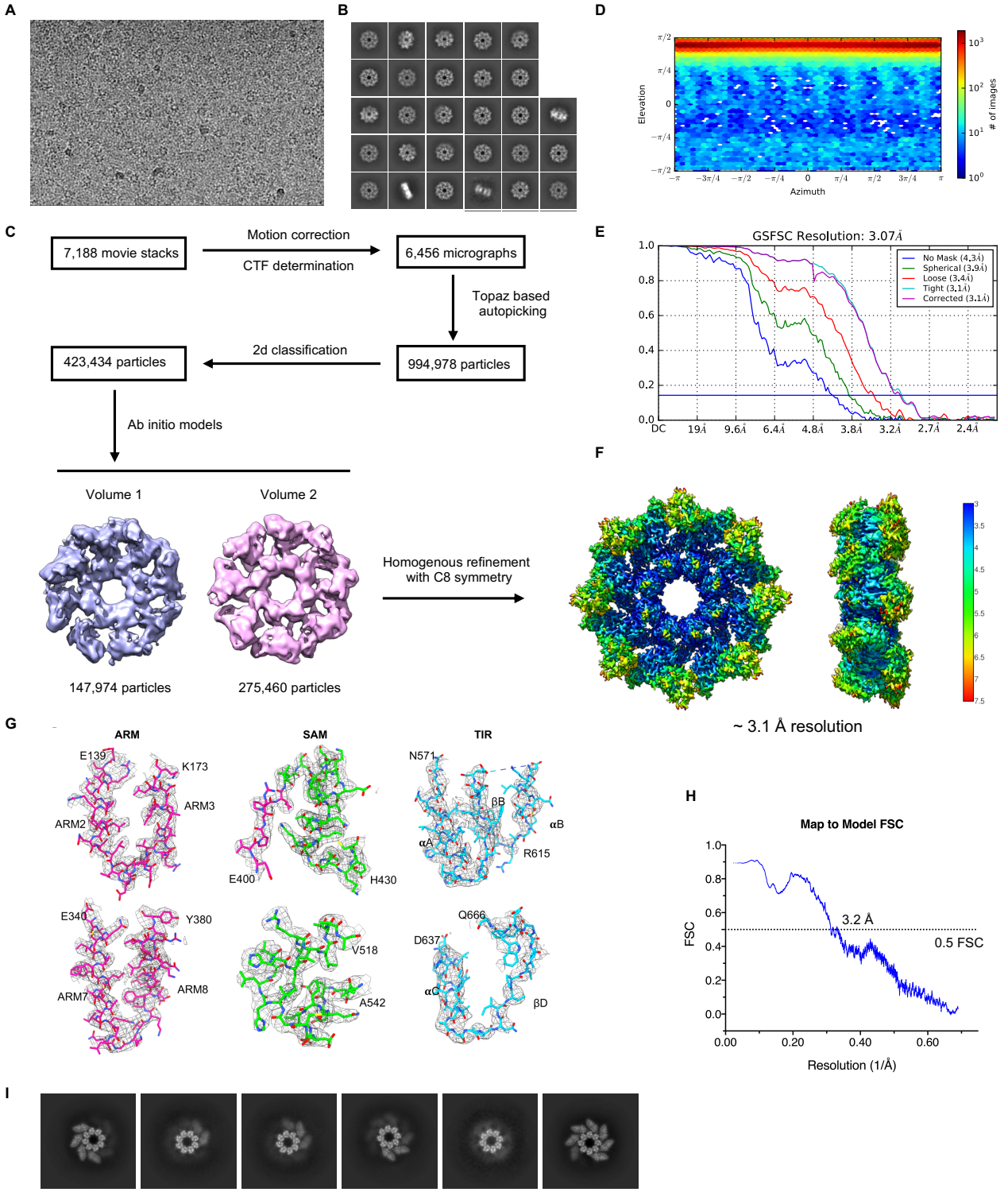

Figure S6: Cryo-EM structure of ligand-free hSARM1 (Related to Figure 5).

A) Representative cryo-EM micrograph of hSARM1. **B)** Representative 2D class averages. **C)** Flow-chart of the cryo-EM processing steps. **D)** Angular distribution plots of the final 3D reconstruction. **E)** Gold-standard FSC curves of the final 3D reconstruction. **F)** Local resolution map. **G)** Representative electrostatic potential density maps for the hSARM1 ARM, SAM and TIR domains. Labelled residues indicate the start and end of the displayed amino acid chain. **H)** Map-to-model FSC curve of the final model and DeepEMhancer post-processed map. **I)** Representative 2D class averages of hSARM1 particles with an incomplete peripheral ARM domain ring.

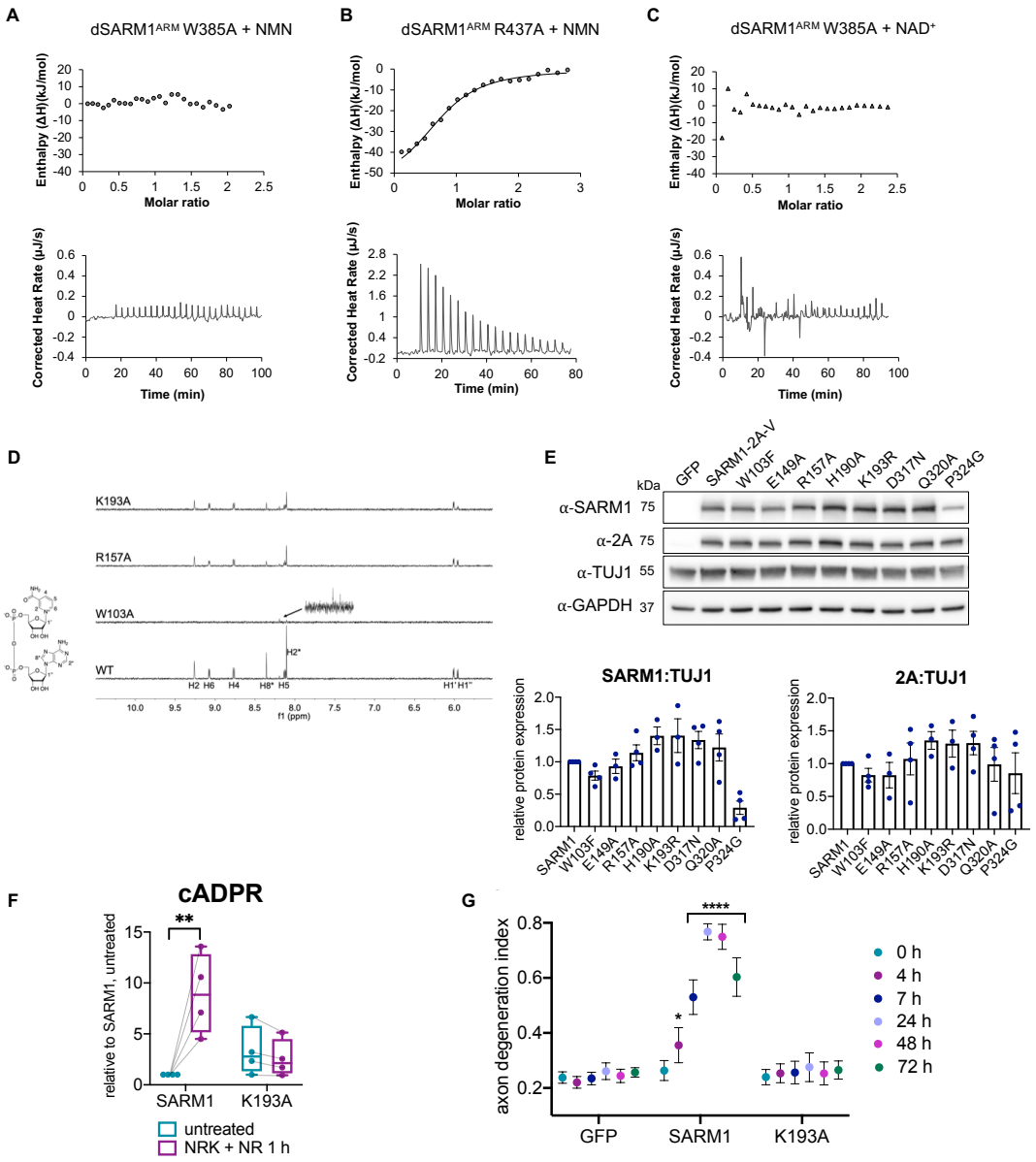

Figure S7: Characterization of hSARM1 NMN-binding pocket mutants (Related to Figure 6).

A) Raw (bottom) and integrated ITC data (top) for the titration of 1 mM NMN with 100 µM dSARM1^{ARM} W385A. **B)** Raw (bottom) and integrated ITC data (top) for the titration of 0.6 mM NMN with 85 µM dSARM1^{ARM} R437A. **C)** Raw (bottom) and integrated ITC data (top) for the titration of 0.7 mM NAD$^+$ with 100 µM dSARM1^{ARM} W385A. **D)** STD NMR spectra showing NAD$^+$ binding to WT and mutant hSARM1 proteins. The protein concentration was 5.25 µM, while the initial NAD$^+$ concentration was 500 µM for all samples. **E)** Representative western blot to detect protein expression of SARM1 after lentiviral expression in primary eDRG neurons from *Sarm1*$^{-/-}$ mice. Quantification of relative protein expression comparing SARM1 to tubulin loading control (TUJ1) and 2A to TUJ1. The SARM1 antibody was generated using a peptide containing P324 and the P324G mutant is poorly detected by this antibody. **F)** cADPR levels from primary eDRG neurons from *Sarm1*$^{-/-}$ mice expressing wild-type or mutant SARM1 and NRK1 from lentivirus, untreated or after 1 h NR [100 µM] treatment, relative to levels from untreated wild-type SARM1 expressing neurons, measured by LC-MS-MS. **G)** Axon degeneration time course after axotomy in primary eDRG neurons from *Sarm1*$^{-/-}$ mice expressing wild-type or mutant SARM1 from lentivirus, quantified as degeneration index (DI), where a DI of 0.35 or above represents degenerated axons. Data correspond to means from replicate experiments and error bars denote ±SEM. Statistical significance was determined by two-way ANOVA with Dunnett's multiple

comparison test, comparing each time-point to time 0 h within each condition. * denotes P value=<0.05; **=<0.01; ***=<0.001; ****=<0.0001.

Table S1: Crystallographic analysis (Related to Figure 4).

Data collection				
	Ligand-free dSARM1^{ARM}	NMN-bound dSARM1^{ARM}	NMN-bound dSARM1^{ARM} (Br soak)	NMN-bound dSARM1^{ARM} (SeMet)
Space group	P1 2_1 1	P1	P1	P1
a, b, c (Å)	63.30, 101.36, 98.57	38.92, 50.79, 76.05	39.07, 51.08, 75.73	38.89, 50.31, 75.22
α, β, γ (°)	90, 103.77, 90	103.52, 101.90, 95.26	103.38, 101.52, 96.66	104.86, 101.36, 94.91
Resolution (Å)	47.87-3.35 (3.61-3.35)	71.88-1.46 (1.60-1.46)	48.97-1.68 (1.82-1.68)	48.12-1.89 (2.11-1.89)
R_{merge}	0.23 (1.36)	0.05 (0.95)	0.08 (1.77)	0.07 (0.76)
R_{meas}	0.32 (1.88)	0.06 (1.15)	0.09 (2.05)	0.09 (1.08)
R_{pim}	0.22 (1.30)	0.03 (0.63)	0.04 (1.01)	0.07 (0.76)
Mean I/σ (I)	4.7 (1.1)	15.9 (1.6)	13.9 (1.0)	9.2 (1.2)
$CC_{1/2}$	1.00 (0.37)	1.00 (0.63)	1.00 (0.40)	1.00 (0.47)
Total reflections	58,693 (11,162)	456,719 (20,265)	393,818 (19,421)	86,502 (4,041)
Unique reflections	17,198 (3,286)	64,028 (3,201)	48,934 (2,447)	24,291 (1,216)
Completeness (spherical)	97.7 (91.1)	67.2 (14.2)	78.2 (19.1)	56.6 (10.0)
Completeness (ellipsoidal)		83.5 (40.3)	90.0 (44.7)	85.3 (38.8)
Multiplicity	3.4 (3.4)	7.1 (6.3)	8.0 (7.9)	3.6 (3.3)
Anomalous completeness (spherical)	91.1 (84.0)	66.5 (14.0)	76.4 (18.5)	55.8 (9.7)
Anomalous completeness (ellipsoidal)		82.7 (39.8)	87.9 (43.4)	84.1 (38.0)
Anomalous multiplicity	1.6 (1.7)	3.6 (3.2)	4.1 (4.1)	1.8 (1.7)
Refinement				
	Ligand-free dSARM1^{ARM}	NMN-bound dSARM1^{ARM}		
Resolution (Å)	47.87-3.35	37.67-1.65		
R_{work}	0.2445	0.2120		
R_{free}	0.2716	0.2295		
RMS bonds (Å)	0.002	0.002		
RMS angles (°)	0.890	0.473		
Ramachandran favored (%)	95.32	98.51		
Ramachandran outliers (%)	0	0.33		
Rotamer outliers (%)	0	0.19		
Clashscore	4.72	1.64		
Average B-factor (Å^2)	90.85	27.77		
C-beta outliers	0	0		

1. The statistics were calculated using AIMLESS (ligand-free) (Evans and Murshudov, 2013), autoPROC (NMN-bound) (Vonrhein et al., 2011) and MolProbity (Williams et al., 2018).

2. The numbers in parentheses represent the highest resolution shell.

3. $R_{merge} = \Sigma_{hkl} \Sigma_j |I_{hkl,j} - < I_{hkl} > | / (\Sigma_{hkl}\Sigma_j I_{hkl,j})$; $R_{meas} = \Sigma_{hkl} [N/(N-1)]^{1/2} \Sigma_j |I_{hkl,j} - < I_{hkl} > | / \Sigma_{hkl}\Sigma_j I_{hkl,j})$; $R_{pim} = \Sigma_{hkl} [1/(N-1)]^{1/2} \Sigma_j |I_{hkl,j} - < I_{hkl} > | / \Sigma_{hkl}\Sigma_j I_{hkl,j})$.

4. $R_{work} = \Sigma_{hkl} |Fobs_{hkl} - Fcalc_{hkl}| / \Sigma_{hkl}|Fobs_{hkl}|$; R_{free} is equivalent to R_{work}, with 5% of data excluded from refinement process. $|Fobs_{hkl}|$ and $|Fcalc_{hkl}|$ represent the observed and calculated structure factor amplitudes, respectively.

Table S2: Proteins structurally similar to dSARM1^{ARM}, based on Dali analysis (Related to Figure 4 and S4).

PDB ID	Z score	RMSD (Å)	Description
6wpk*	29.2	2.9	NAD(+) hydrolase SARM1
1wa5	17.1	2.7	Kap60p (importin-alpha)
6sa8	15.7	3.4	Ring-like fusion protein with designed armadillo and ankyrin repeats
6kbn	15.4	5.5	Vacuolar protein 8
5xgc	15.4	3.3	Small GTPase-GDP dissociation stimulator-558 (SmgGDS-558)
3nmz	15.3	2.5	Adenomatous polyposis coli (APC)
4r0z	15.0	3.3	β-Catenin homolog HMP-2
1xqr	15.0	4.2	Hsp70 binding protein 1 (HspBP1)
3l6x	14.8	3.2	p120 isoform 4A
5ewp	14.4	2.9	Armadillo repeats only protein from *Plasmodium falciparum*
4k6j	13.8	3.3	Wings apart-like protein (Wapl)
5lsw	13.7	3.8	Roquin CAF40
6u62	13.6	3.0	Mechanistic target of rapamycin complex 1 (mTORC1)
4hm9	13.5	3.1	Beta-catenin-like protein 1
3opb	13.4	3.5	Swi5-dependent HO expression protein 4 (She4p)
3gq2	13.2	3.8	p115
3ebb	13.0	4.1	Phospholipase A2-activating protein (PLAA)
3c2g	12.7	3.7	Sys-1 protein
6tc0	12.7	3.2	MMS19 nucleotide excision repair protein homolog
6hb3	12.6	3.4	Hgh1
4g3a	12.6	4.4	Microtubule-associated protein Mast/Orbit
2xwu	12.6	4.2	Importin13
6lth	12.6	2.9	AT-rich interactive domain-containing protein 1A
5z58	12.5	5.8	Splicing factor 3B subunit 1
4i2w	12.2	3.4	UNC-45

*ARM domain from the published cryo-EM structure of SARM1 (Bratkowski et al., 2020).

Table S3: NMN-interacting residues in *Drosophila* and human SARM1, based on the dSARM1^{ARM} crystal structure (Related to Figure 4).

hSARM1	dSARM1	Region	Interacting moiety of NMN
W103	W385	1	Nicotinamide
R110	H392	1	Nicotinamide
Q114	Y396	1	Phosphate
E149	E429	2	Ribose
Q150	Q430	2	Ribose
I151	C431	2	Ribose
L152	L432	2	Ribose
V153	T433	2	Ribose
A154	T434	2	Ribose
R157	R437	2	Phosphate
H190	H473	3	Phosphate
K193	K476	3	Phosphate
S316	L595	4	Nicotinamide
D317	A596	4	Nicotinamide
T318	H597	4	Nicotinamide
S319	A598	4	Nicotinamide
Q320	H599	4	Nicotinamide
G321	G600	4	Nicotinamide
R322	Q601	4	Nicotinamide
G323	S602	4	Phosphate

Table S4: Cryo-EM analysis (Related to Figure 5 and S6).

	hSARM1$^{28-724}$
Data collection and processing	
Microscope	Titan Krios
Detector	Gatan K3 direct electron detector
Voltage (kV)	300
Nominal magnification	81,000
Super resolution pixel size (Å)	0.543
Binned pixel size (Å)	1.09
Defocus range (μm)	-1.5 to -2.7
Total exposure (e/Å^2)	54
Exposure per frame (e/Å^2)	1.2
Total micrographs (no.)	7188
Total extracted particles (no.)	4,958,973
Final particles (no.)	275,460
Symmetry imposed	C8
Map sharpening B-factor (Å^2)	N/A
Resolution (FSC)	
Masked (0.143/0.5)	3.1
Unmasked (0.143/0.5)	4.3
Model composition	
Number of chains	8
Atoms	36,976 (hydrogens: 0)
Residues	4720
Water	0
Ligands	0
Model validation	
Bonds (RMSD)	
Length (Å) (> 4σ)	0.006 (0)
Angles (°) (> 4σ)	0.646 (0)
MolProbity score	1.88
Clash-score	8.80
Ramachandran plot (%)	
Outliers	0
Allowed	6.14
Favored	93.86
Rotamer outliers (%)	0
Cß≤ outliers (%)	0
Peptide plane (%)	
Cis proline/general	0.0/0.0
Twisted proline/general	0.0/0.0
CaBLAM outliers (%)	1.59
ADP B-factor (min/max/mean; Å^2)	35.02/143.92/76.97
Occupancy = 1 (%)	100
Map to model FSC (0.143/0.5, Å)	1.9/3.1
Map correlation coefficient	0.75

The statistics were calculated using CryoSPARC (Punjani et al., 2017) and the phenix.validation_cryoem tool (Williams et al., 2018).